bioRxiv preprint doi: https://doi.org/10.1101/055533; this version posted August 25, 2017. The copyright holder for this preprint (which was not certified by peer review) is the author/funder, who has granted bioRxiv a license to display the preprint in perpetuity. It is made available under aCC-BY 4.0 International license.

Living Neural Networks: Dynamic Network Analysis of Developing Neural Progenitor Cells

Arun S. Mahadevan[1], Nicolas E. Grandel[3], Jacob T. Robinson[1,2], Amina A. Qutub[1*]

[1]Department of Bioengineering, [2]Department of Electrical and Computer Engineering, Rice University, Houston, Texas, 77005, U.S.A., [3]Stanford University, California 94305

[*]Contact: amina@rice.edu

ABSTRACT

The architecture of the mammalian brain has been characterized through decades of innovation in the field of network neuroscience. However, the assembly of the brain from progenitor cells is an immensely complex process, and a quantitative understanding of how neural progenitor cells (NPCs) form neural networks has proven elusive. Here, we introduce a method that integrates graph-theory with long-term imaging of differentiating human NPCs to characterize the evolution of spatial and functional network features in NPCs during the formation of neuronal networks in vitro. We find that the rise and fall in spatial network efficiency is a characteristic feature of the transition from immature NPC networks to mature neuronal networks. Furthermore, networks at intermediate stages of differentiation that display high spatial network efficiency also show high levels of network-wide spontaneous electrical activity. These results support the view that network-wide signaling in immature progenitor cells gives way to a hierarchical form of communication in mature neural networks. The Living Neural Networks method bridges the gap between developmental neurobiology and network neuroscience, and offers insight into the relationship between developing and mature neuronal networks.

bioRxiv preprint doi: https://doi.org/10.1101/055533; this version posted August 25, 2017. The copyright holder for this preprint (which was not certified by peer review) is the author/funder, who has granted bioRxiv a license to display the preprint in perpetuity. It is made available under aCC-BY 4.0 International license.

INTRODUCTION

The study of complex, multiscale brain networks using concepts from graph theory and network science – an approach collectively termed network neuroscience – has enabled significant insight into the structural and functional organization of the brain[1,2]. Micro-connectomics – the study of organizational principles of neuronal networks at the cellular scale[3,4], is an important subset of complex brain networks that has yielded insight into architectural features of the nervous system at the level of their basic building blocks. A number of studies have applied graph-theoretic approaches to study the functional and anatomical connectivity of *in vitro* neuronal cultures formed from dissociated cells[5–7]. These studies have shown, for instance, that in vitro neuronal networks self-assemble in a small-world topology with high clustering and low path length. Micro-connectomic analyses of slice cultures[8,9], and more recently, large-scale network reconstructions[10], have revealed fundamental properties of mammalian cortical networks, such as long-tailed synaptic connectivity, the presence of preferentially connected subgroups of neurons and overrepresentation of certain network motifs. However, despite the progress made in understanding the fundamental architectural features of neuronal networks, no models have been available to study the development of human neural networks from progenitor cells in a quantitative manner, nor have there been tools to simultaneously characterize the dynamics of human neuronal networks spatially and functionally at the cellular level.

Cell-cell communication among neural progenitor cells (NPCs) is an essential aspect of human nervous system development. Neural progenitor cells cluster together in specialized microenvironments or niches where communication with neighboring cells plays an important role in determining cell behavior[11]. Prior to the formation of functional synapses, NPCs display structured intercellular communication that plays a critical role in the spatiotemporal control of self-renewal and differentiation, and shapes developing neural circuits. Examples of structured cell-cell communication include patterned, spontaneous electrical

bioRxiv preprint doi: https://doi.org/10.1101/055533; this version posted August 25, 2017. The copyright holder for this preprint (which was not certified by peer review) is the author/funder, who has granted bioRxiv a license to display the preprint in perpetuity. It is made available under aCC-BY 4.0 International license.

activity mediated partly through gap junctional coupling[12–14], maintenance of intercellular configurations through tight junction proteins[15] and control of cell differentiation through Notch signaling[16,17]. Notably, the predominant forms of communication employed by NPCs can be described as juxtacrine signaling, i.e., requiring direct cell-cell contact. This is in contrast to communication in mature neuronal networks, where the physical wiring among neurons is important and network-wide information is conveyed primarily through synaptic contacts. Given the dominance of juxtacrine modes of signaling among progenitor cells, graph-theoretic approaches need to be modified to study developing neural networks.

To enable the bridge between development and network neuroscience, we harness another emerging technology: human stem cell engineering. In recent years, significant advances in stem cell differentiation protocols have made it possible to produce a multitude of neuronal types and have provided a standardized workflow for generating functional human neurons in vitro[18]. The ubiquity of stem cell differentiation protocols provides a unique opportunity to study the self-assembly of neuronal networks in a dish.

In this report, we introduce a method to study network features of developing human neural networks. We use long-term imaging coupled with automated image analysis to develop network representations of cell spatial topology. A schematic representation of our experimental paradigm is shown in **Figure 1**. We use our method to demonstrate that two independent human NPC cell lines exhibit a similar rise and fall in spatial network efficiency that characterizes the maturation of in vitro neural networks. Further, we demonstrate that high network efficiencies at intermediate stages of neural differentiation are linked with high levels of spontaneous electrical activity. The paradigm presented here can be used to uncover fundamental features of neuronal network formation from progenitor cells. More broadly, the Living

bioRxiv preprint doi: https://doi.org/10.1101/055533; this version posted August 25, 2017. The copyright holder for this preprint (which was not certified by peer review) is the author/funder, who has granted bioRxiv a license to display the preprint in perpetuity. It is made available under aCC-BY 4.0 International license.

Neural Networks method enables studies of how spatial dynamics of human neural cells link to neuron-specific functions.

RESULTS

Functional characterization and spatial network representation of differentiating NPC cultures

In the first part of this study, we used primary hNP1 neural progenitor cells derived from H9 human embryonic stem cells. These cells were maintained as undifferentiated, mitotic progenitor cells in the presence of basic fibroblast growth factor (bFGF). Withdrawal of growth factors from culture medium was used to induce spontaneous differentiation of hNPCs[19].

First, we performed immunocytochemistry and whole-cell patch clamp electrophysiology experiments to uncover the time course of functional development in differentiating hNP1 cells. Cells at day 0 stained positively for Nestin, a Type VI intermediate filament expressed by dividing neural progenitor cells (**Figure 2a**). Cells at day 14 were positive for microtubule-associated protein-2 (MAP2), a protein associated with

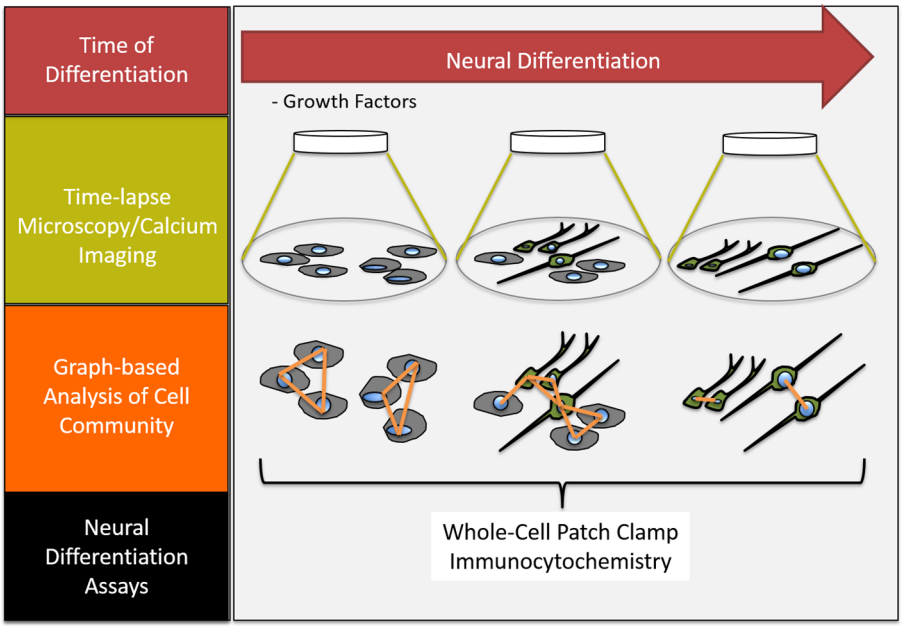

Figure 1. Schematic of the Living Neural Networks paradigm

bioRxiv preprint doi: https://doi.org/10.1101/055533; this version posted August 25, 2017. The copyright holder for this preprint (which was not certified by peer review) is the author/funder, who has granted bioRxiv a license to display the preprint in perpetuity. It is made available under aCC-BY 4.0 International license.

dendrite formation in maturing neurons (**Figure 2b**). Analysis of peak inward and outward currents from voltage-clamp experiments showed that cells at all time points exhibited the same levels of outward currents, but showed increasing magnitudes of inward currents (**Figure 2c, d**). Inward currents are typically driven by voltage-gated sodium channels, and their presence indicates a more mature neuronal

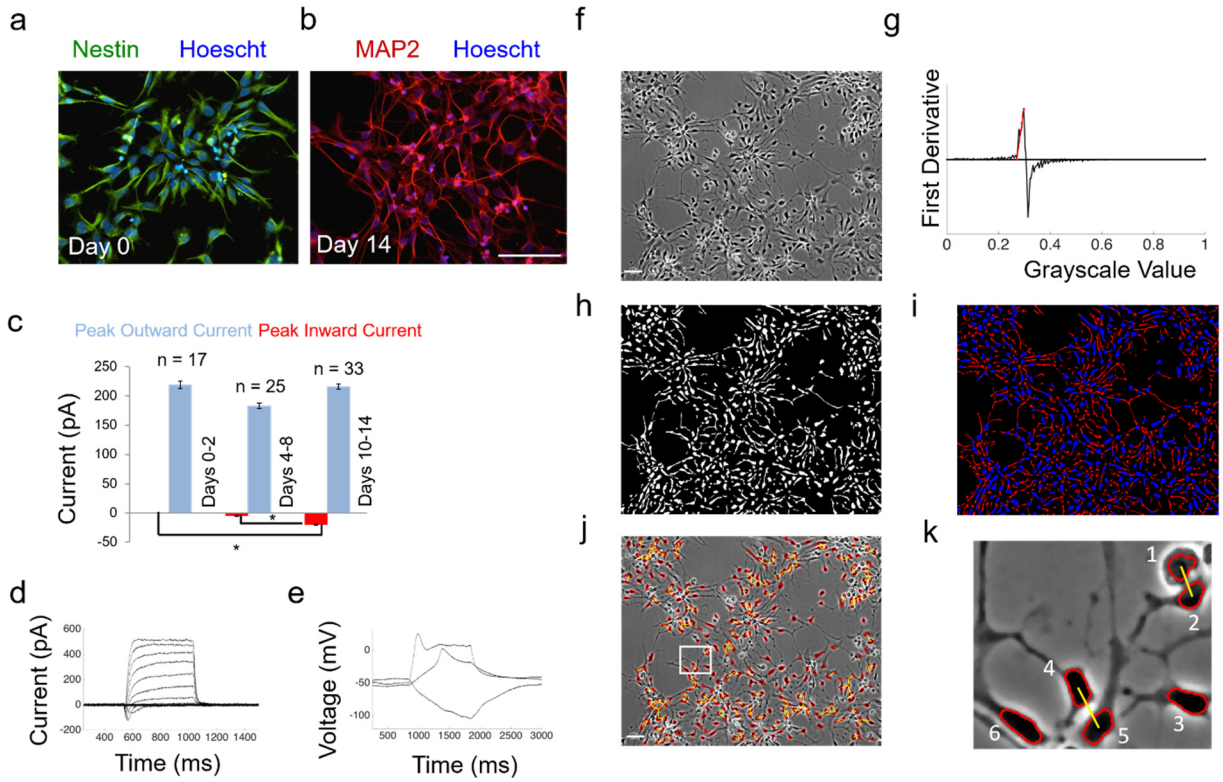

Figure 2. Functional characterization and spatial network representation of differentiating NPCs. (a) hNP1 cells at day 0 stain positively for Nestin. **(b)** Cells at day 14 stain positive for MAP2. In (a-b) nuclei are labeled by Hoescht; scale bar = 100 µm. **(c)** Peak inward and outward currents determined through whole-cell patch clamp electrophysiology. Number of cells recorded (n) is shown above the bar for each time period. Error bars represent SEM; *p < 0.05 from two-sample t-test. **(d)** Weak action potentials evoked from a cell at day 14 through current injection. Magnitudes of current injected are -30pA, +20pA and +120pA from holding. **(e)** Voltage-gated inward and outward currents seen in the same cell. Voltage steps applied were from -60mV to +90mV in 10mV increments**. (f)** Representative phase contrast image of hNP1 cells, shown at day 3; scale bar = 50 µm. **(g)** First derivative of the pixel intensity histogram, with a linear fit to the ascending portion shown as a red line. The point where this line met the x-axis was used as a threshold for segmentation. **(h)** Binary image obtained upon thresholding the grayscale image. **(i)** Separation of linear features through morphological opening of the binary image yields cell bodies (blue) and neurites (red). **(j)** Phase contrast image from (f) with soma boundaries overlaid in red, and proximity edges shown in yellow. **(k)** Inset from (j) showing six soma, of which two pairs (1, 2) and (4, 5) are connected by proximity edges; the intercellular distance for these two pairs are smaller than their average diameter multiplied by a scaling factor S = 2; Soma 3 and 6 are isolated nodes since they are not sufficiently close to any other soma. All microscope images are displayed with enhanced contrast for easy visualization.

bioRxiv preprint doi: https://doi.org/10.1101/055533; this version posted August 25, 2017. The copyright holder for this preprint (which was not certified by peer review) is the author/funder, who has granted bioRxiv a license to display the preprint in perpetuity. It is made available under aCC-BY 4.0 International license.

phenotype. Furthermore, weak action potentials could be elicited from cells showing inward currents at later time points (3/11 cells at day 14) through current injection (**Figure 2e**). These experiments showed that Nestin-positive hNP1 cells matured over 14 days to MAP2-positive neurons, with neuronal fate commitment occurring between days 4-8, indicated by the appearance of neuronal phenotypes in that time period.

In order to uncover topological changes in differentiating hNP1 cells, we combined long-term imaging of differentiating cultures with a graph-based approach for quantifying cell community structure. We conducted two biologically independent experiments where cultures were imaged at days 0, 3, 6, 9, 12 and 14 after withdrawal of bFGF. An additional dataset was obtained by imaging differentiating cultures at 1-hour intervals for a total duration of 8 days (**Supplementary Video 1**). Selected image sequences were analyzed using custom image-processing algorithms, resulting in the extraction of soma and neurites for each phase-contrast image (**Figure 2f-i**) (see Methods for details).

We built network representations of spatial topology by denoting soma as nodes and using spatial proximity between soma to assign edges (**Figure 2j, k**). The resulting adjacency matrix, A, represented the spatial topology of cells, where $A_{i,j} = 1$ if an edge existed between cells i and j, and 0 otherwise. In this manner, we constructed non-weighted, undirected graphs representing hNP1 communities from microscope images (**Supplementary Video 2**).

Structure and information flow in NPC spatial graphs

In order to describe the structure and topology of hNP1 spatial graphs, we evaluated a number of metrics derived from graph theory. **Table 1** lists 16 metrics that were computed and normalized appropriately to account for network size[20]. The network metrics provide information on various aspects of the graph

bioRxiv preprint doi: https://doi.org/10.1101/055533; this version posted August 25, 2017. The copyright holder for this preprint (which was not certified by peer review) is the author/funder, who has granted bioRxiv a license to display the preprint in perpetuity. It is made available under aCC-BY 4.0 International license.

structure such as information flow, connectivity and abundance of motifs. **Figure 3a** shows the covariance matrix of all 16 metrics as a hierarchically clustered heatmap. The heatmap shows several strong positive correlations among degree-related metrics like average degree, average neighbor degree and their variances. Interesting negative correlations include those between network efficiency and number of connected components, and between clustering coefficient and all degree-related metrics. In the following section, we focus on metrics that have intuitive biological interpretations, their trends across time of differentiation, and relationships observed with other metrics that explain these trends. Trends in metrics not discussed in the main text are shown in **Supplementary Figure 4**.

Network efficiency and clustering coefficient are commonly used measures of efficiency in global and local information flow[21] (**Table 1**). When applied to hNP1 networks, these metrics describe the efficiency of information exchange at the network-wide and local neighborhood levels respectively, through cell body proximity (compared to random graphs obtained through degree-preserving rewiring (**Supplementary Figure 3**)). In this context, information exchange could include flow of ions through gap junctions or the diffusion of chemical signals from cell to cell. Evaluation of these metrics in hNP1 networks sampled across 30 different locations from two biologically independent experiments showed that network efficiency increased from day 0 to day 6, and then decreased from days 6 to 14, while clustering coefficient rose constantly from day 0 to 14 (**Figure 3b,c**). Thus, there appears to be a transition from topologies favoring global information flow to those favoring a hierarchical form of communication, occurring from day 6 – 14 of differentiation.

Table 1. Metrics computed, their descriptions, and mode of normalization to account for the network size. n = number of nodes, m = number of edges.

Graph Metrics	Shorthand	Definition	Normalization
Network Density	NetworkDensity	Average degree of graph, normalized by total maximum possible degree $$\text{NetworkDensity} = \frac{2m}{n(n-1)}$$	Maximum possible degree, $(n-1)$
Variance in Degree	varK	Variance of normalized node degree sequence	Node degree sequence normalized by maximum possible degree, (n-1)
Average Neighbor Degree	avgeK_neighbor	Average degree of node neighborhood, across all nodes	Maximum possible degree, (n-1)
Variance in Neighbor Degree	varK_neighbor	Variance of the normalized average neighbor degree sequence	-
Network Efficiency	NetworkEfficiency	The average reciprocal of shortest path length across all pairs of nodes, E	Average network efficiency of 100 random graphs generated through degree-preserving rewiring, E_{rand}. Random graph generation is illustrated in **Supplementary Figure 3.**
Average Clustering Coefficient	ClusteringCoefficient	Fraction of total possible links among the neighbors of a node that are actually present, averaged across all nodes, C	Average clustering coefficient of 100 random graphs generated through degree-preserving rewiring, C_{rand}
Number of connected components	nConnectedComponents	Number of disconnected sub-graphs in main graph	-
Average Size of Connected Components	AvgeComponentSize	Average number of nodes in each connected component	Total nodes, n
Variance in size of connected components	VarComponentSize	-	-

bioRxiv preprint doi: https://doi.org/10.1101/055533; this version posted August 25, 2017. The copyright holder for this preprint (which was not certified by peer review) is the author/funder, who has granted bioRxiv a license to display the preprint in perpetuity. It is made available under aCC-BY 4.0 International license.

Network Diameter	NetworkDiameter	Longest shortest path length of network	Longest possible path, (n-1)
Triangular loop count	nLoops3	Number of loops of 3 nodes	Total possible number of triplets, ${}^{n}C_3$
4-star motif Count	nStar4	Number of star motifs with one hub and three spokes	Total possible number of 4-tuples, ${}^{n}C_4$
5-star motif count	nStar5	Number of star motifs with one hub and four spokes	Total possible number of 5-tuples, ${}^{n}C_5$
6-star motif count	nStar6	Number of star motifs with one hub and five spokes	Total possible number of 6-tuples, ${}^{n}C_6$
Rich-Club Metric Average	AvgeRichClubMetric	Measure of the tendency of nodes with high number of links to be well connected among each other[22]; Computed for threshold degrees between 1 and (n-1)	Average Rich-Club Metric of 100 random graphs generated through degree-preserving rewiring, RCM_{rand}
Assortativity	Assortativity	Pearson correlation coefficient of degrees between pairs of linked nodes[23].	-

135

bioRxiv preprint doi: https://doi.org/10.1101/055533; this version posted August 25, 2017. The copyright holder for this preprint (which was not certified by peer review) is the author/funder, who has granted bioRxiv a license to display the preprint in perpetuity. It is made available under aCC-BY 4.0 International license.

bioRxiv preprint doi: https://doi.org/10.1101/055533; this version posted August 25, 2017. The copyright holder for this preprint (which was not certified by peer review) is the author/funder, who has granted bioRxiv a license to display the preprint in perpetuity. It is made available under aCC-BY 4.0 International license.

136

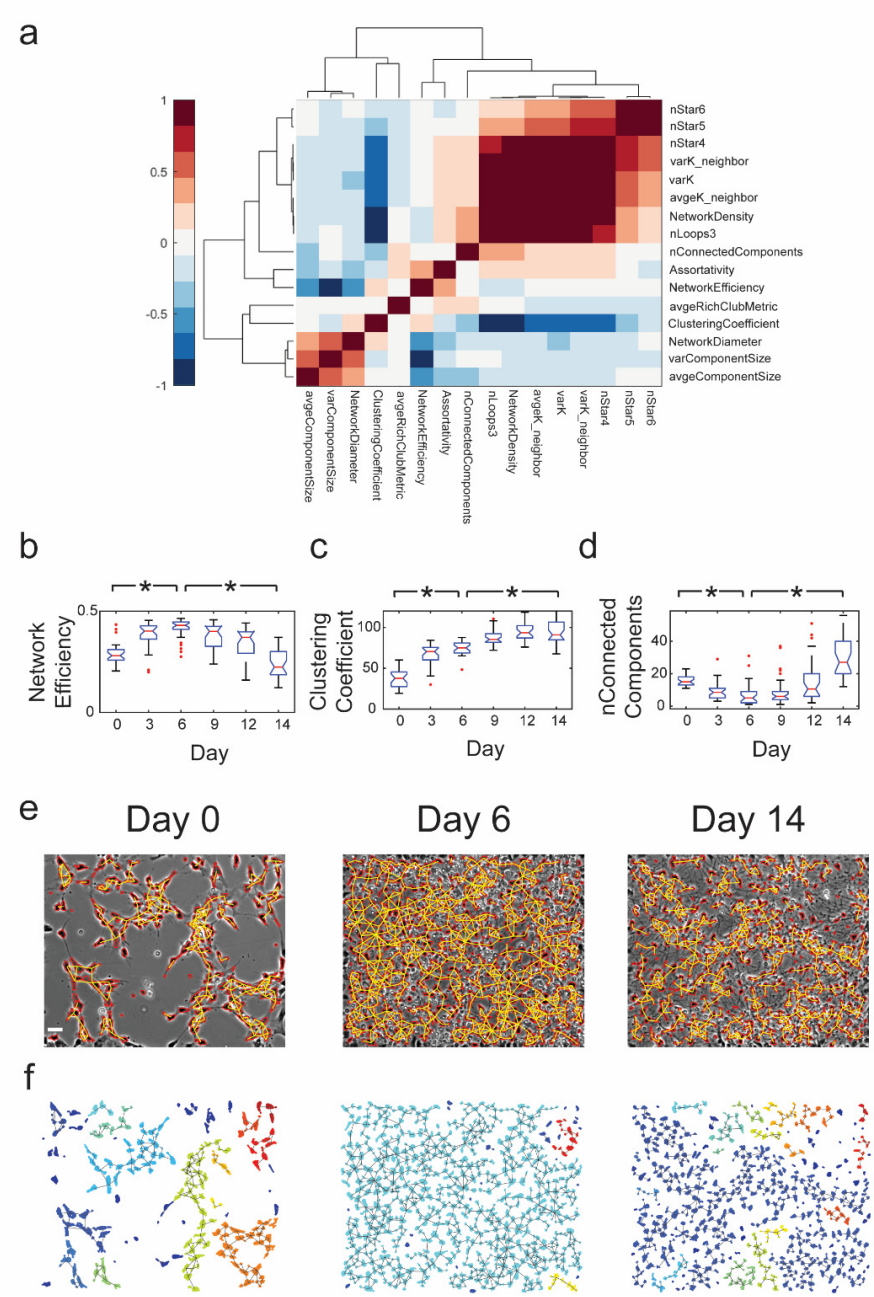

Figure 3. Spatial network efficiency is highest at intermediate stages of differentiation. (a) Correlation heatmap of all metrics obtained by hierarchical clustering of the covariance matrix. Legend shows Pearson correlation coefficient values. Rows and columns are labeled with shorthand for metrics (Table 1). (b) Box plot of network efficiency across time. (c) Box plot of clustering coefficient across time. (d) Box plot of number of connected components across time. (e) Spatial graph representations of images taken at day 0, day 6 and day 14. Soma are outlined in red and edges are shown in yellow; scale bar = 50 µm. (f) Cell bodies from the images in (e), with each connected component labeled with distinct colors. For box plots in (b-d), red notches represent median ($Q2$), length of boxes represent interquartile range (IQR), length of notches represent $Q2 \pm \left(1.57 \times IQR/\sqrt{n}\right)$, whiskers represent $Q1 - (1.5 \times IQR)$ and $Q3 + (1.5 \times IQR)$ and red circles represent outliers. $Q1$ = 25th percentile, $Q2$ = median, $Q3$ = 75th percentile, $n = 30$ data points for each box plot. * p < 0.005 from Wilcoxon signed rank test.

bioRxiv preprint doi: https://doi.org/10.1101/055533; this version posted August 25, 2017. The copyright holder for this preprint (which was not certified by peer review) is the author/funder, who has granted bioRxiv a license to display the preprint in perpetuity. It is made available under aCC-BY 4.0 International license.

The correlation heatmap in **Figure 3a** showed a strong negative correlation between network efficiency and number of connected components in the graph. The number of connected components (**Figure 3d**) is a count of the number of disconnected sub-graphs in the main network and is a measure of the connectivity of the graph – a graph with a high number of connected components has a low connectivity. NPC networks at day 0, 6, and 14 are shown in **Figure 3e** and the corresponding connected components are shown in **Figure 3f**. From these images, it is clear that the formation of a giant connected component due to cell proliferation up to day 6 leads to an increase in the connectivity of the network, which in turn causes an increase in network efficiency. The subsequent disaggregation of the large component into smaller modules from days 6 to 14 contributes to the decrease in efficiency seen in that time period.

Development of Functional and Spatial Networks

We next probed the relationship between functional and spatial networks in developing NPCs, using ReNcell VM immortalized human neural progenitor cells. Differentiation induced by growth factor withdrawal in this cell line led to the formation of dense networks within 5 days. Differentiated cultures contained neurons and glia expressing the classic markers β(III) tubulin and GFAP respectively (**Supplementary Figure 6**).

We performed calcium imaging using the fluorescent calcium indicator Fluo-4 to record spontaneous activity in developing cultures at days 1, 3 and 5, and employed cross-correlation analysis to infer functional connectivity in the networks (**Figure 4a**, **Supplementary Figure 7**). Analysis of functional networks revealed that cultures at day 3 had significantly more activity than those at days 1 and 5, as measured by the fraction of active cells (**Figure 4b, Supplementary Videos 3-5**). Interestingly, the functional network was not restricted to cells with short intercellular distances, with cells in the whole field of view having highly correlated calcium activity (**Figure 4c**).

bioRxiv preprint doi: https://doi.org/10.1101/055533; this version posted August 25, 2017. The copyright holder for this preprint (which was not certified by peer review) is the author/funder, who has granted bioRxiv a license to display the preprint in perpetuity. It is made available under aCC-BY 4.0 International license.

161 We next built spatial graphs using nucleus images from the same cultures in which calcium imaging was

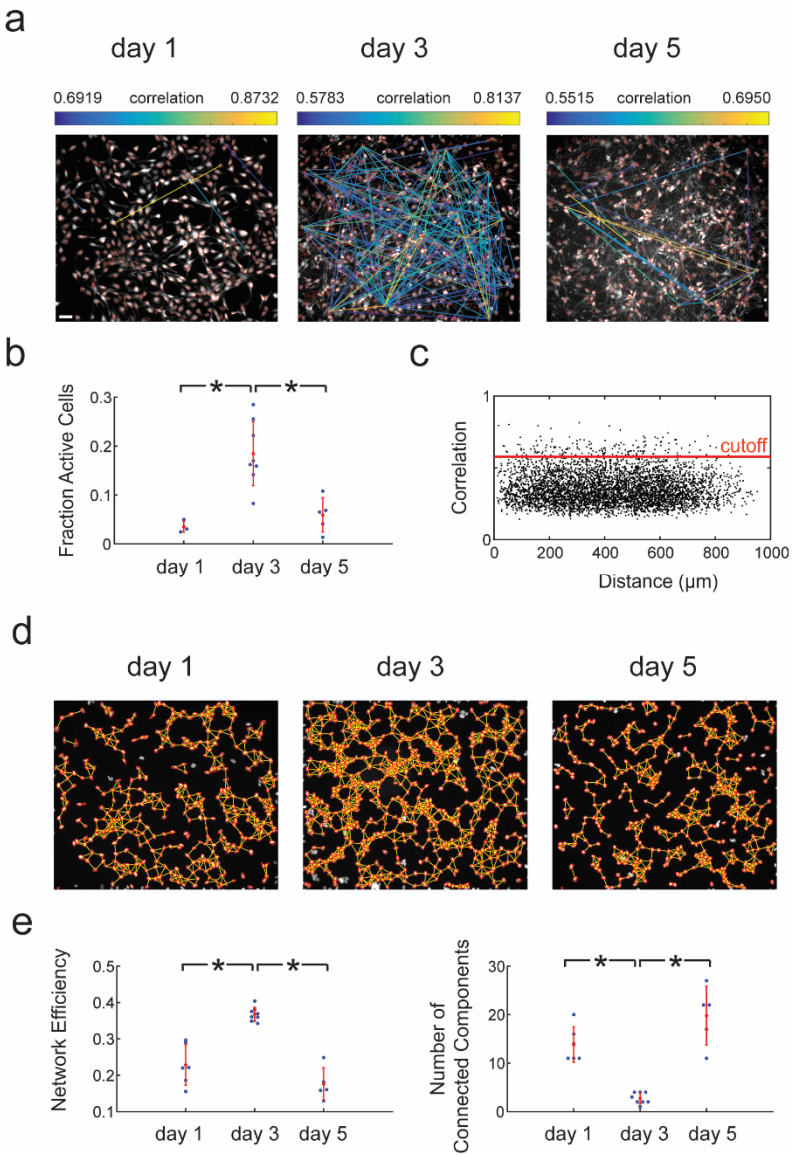

Figure 4. Functional and spatial networks in ReNcell VM NPCs. (a) Functional networks obtained through calcium imaging with Fluo-4 in developing NPC networks at days 1, 3 and 5. Correlations between cells are shown as a network plot overlaid on the maximum intensity image from calcium image sequences; scale bar = 50 μm **(b)** Fraction of active cells in the network. Active cells are defined as cells whose normalized fluorescence traces have three or more calcium transients. **(c)** Plot of correlation versus intercellular distance for day 3 network shown in (a). Correlation threshold generated from shuffled dataset is shown as a red line. **(d)** Spatial networks overlaid on immunofluorescence images of nuclei stained with Hoescht dye; scaling factor = 3. The nucleus images correspond to the images shown in (a). **(e)** Network efficiency of spatial networks peaks at day 3. Number of connected components shows the inverse trend. Sample sizes: Day 1 (n=5); Day 3 (n=8); Day 5 (n=5) for all plots. Red notches show mean and standard deviation; *$p < 0.005$ from two-sample t-test. All microscope images are displayed with enhanced contrast for easy visualization.

bioRxiv preprint doi: https://doi.org/10.1101/055533; this version posted August 25, 2017. The copyright holder for this preprint (which was not certified by peer review) is the author/funder, who has granted bioRxiv a license to display the preprint in perpetuity. It is made available under aCC-BY 4.0 International license.

performed (**Figure 4d**). Spatial networks were most efficient at day 3, with the fewest number of connected components (**Figure 4e**). The rise and fall of network efficiency in ReNcell networks mirrored the trends seen in hNP1 networks, with the time course of the trends indicative of network maturation. Further, the peak in spatial network efficiency coincided with the most active functional networks. This leads us to conclude that the high spatial efficiency of NPC networks at intermediate time points of differentiation facilitates high levels of network-wide spontaneous activity.

DISCUSSION

Topological and functional analysis of *in vitro* neuronal networks has the potential to uncover basic organizational principles of their *in vivo* counterparts. Our study provides a new approach which leverages stem cell technology to study the self-assembly of in vitro neuronal networks from neural progenitor cells. We quantified the spatial organization of immature neural cells during differentiation, using a unique application of graph theory. The experimental paradigm presented here enabled us to uncover relationships between spatial topology of NPC communities and functional maturation of developing neural circuits, and allowed us to develop hypotheses about the role of certain topologies on NPC function.

Because chemical and electrical signaling between neural progenitor cells often involves direct contact between adjacent cells, we expect spatial cell organization to be an important aspect of neural development. Two examples where spatial organization would play a role include Notch/Delta signaling and gap junctional communication between cells. The Notch/Delta signaling pathway, which influences the proliferation and neuronal fate commitment of progenitor cells[24,25], is an example of juxtacrine chemical signaling. The canonical Notch signaling pathway functions through the binding of a transmembrane ligand on one cell with the transmembrane receptor on a contacting cell, resulting in the

bioRxiv preprint doi: https://doi.org/10.1101/055533; this version posted August 25, 2017. The copyright holder for this preprint (which was not certified by peer review) is the author/funder, who has granted bioRxiv a license to display the preprint in perpetuity. It is made available under aCC-BY 4.0 International license.

release of the notch intracellular domain (NICD) to initiate downstream signaling cascades in the contacting cell[26]. In addition, immature neural circuits are known to display spontaneous electrical activity, which is an important aspect of their proper development[13,14]. Gap junctions or electrical synapses allow direct access between cells and result in exchange of ions and growth factors, and these are known to be important in the propagation of spontaneous electrical activity. Indeed, neural progenitor cells have been shown to display structured and synchronous calcium activity, dependent on gap junctions and which promotes cell proliferation[12]. More broadly, structured cell-cell communication has been implicated in coordinated chemosensing[27] and migration during development[28]. Thus, the methods of cell-cell communication employed by immature neural cells indicate the significance of spatially organized electrical and chemical signaling.

We found that the rise and fall in spatial network efficiency was a reproducible feature in NPC networks, and believe this is a characteristic feature of the transition from immature NPC networks to mature neuronal networks. Global network efficiency is low in proliferating NPC topologies, rises to a peak in intermediate cultures, and then drops off as cells mature into neuronal networks. The trend in network efficiency is intuitively explained by its negative correlation with the number of connected components, a measure of cell connectivity. Cell proliferation in the early stages of differentiation causes the merging of many disconnected clusters of cells into a giant connected component, which leads to a rise in the overall spatial connectivity and reduction in the average path length. The reorganization of the giant component into smaller modules at later stages leads to a reduction in network efficiency.

Significantly, the peak in spatial network efficiency coincides with the appearance of electrophysiologically mature neurons in culture and high levels of spontaneous network-wide calcium activity respectively in the two different cell lines we studied. Additionally, levels of spontaneous activity drop off in more mature

bioRxiv preprint doi: https://doi.org/10.1101/055533; this version posted August 25, 2017. The copyright holder for this preprint (which was not certified by peer review) is the author/funder, who has granted bioRxiv a license to display the preprint in perpetuity. It is made available under aCC-BY 4.0 International license.

cultures which have significant neurite outgrowth and more clustered cell bodies. The spatial and functional architecture of mature cultures is consistent with previous evidence of highly clustered units developing in neuronal cultures[5–7]. The reduction in network-wide spontaneous activity in more mature cultures is consistent with a transition from a global to a hierarchical structure of communication.

In this study, we show that network analysis provides unique information about the structure of neural progenitor cell communities at the local and global levels. It remains to be seen whether spatial topology of developing cultures is predictive of synaptic connectivity in mature neuronal networks. Several *in vivo* studies have provided evidence for a structure-functional relationship between adult neuronal wiring and the spatiotemporal origin of the constituent neurons. For example, sister excitatory neurons in the neocortex are more likely to develop synapses with each other rather than with other cells[29], and the electrophysiological phenotypes of GABAergic interneurons have been shown to be dependent on the time and place of their birth[30]. Thus, the analysis of spatial topology in developing neuronal circuits in a controlled setting has the potential to uncover structure-function relationships in the resulting mature neural circuits.

The present study also lays the foundation for analysis of the role of cellular neighborhood on cell fate determination of individual progenitor cells. The expression of cell-fate determination factors such as bHLH transcription factors like Hes1 and Ngn2, and proteins involved in cell-cell communication pathways such as Notch/Delta proteins, have been shown to be tightly coupled with each other[17,31]. Computational modeling studies have predicted that Notch-Hes1 intercellular signaling affects differentiation and cell cycle progression of individual cells and this signaling is important for the maintenance of an optimal balance between differentiating cells and self-renewing progenitor cells[32]. The spatial dynamics of cell-cell signaling and its impact on single-cell differentiation status is an intriguing subject for future study.

bioRxiv preprint doi: https://doi.org/10.1101/055533; this version posted August 25, 2017. The copyright holder for this preprint (which was not certified by peer review) is the author/funder, who has granted bioRxiv a license to display the preprint in perpetuity. It is made available under aCC-BY 4.0 International license.

In conclusion, we present a multiplexed approach integrating long-term imaging, automated image analysis, and graph theory to quantify the spatial and functional networks of neural progenitors during neuronal differentiation. The Living Neural Networks method introduces a tangible means to test theories about different forms of neural cell communication and their role in shaping functional neuronal networks. Insights from this study help further our understanding of the fundamental design features of the brain.

METHODS

Cell culture. Human neural progenitor cells (hNP1) derived from H9 human embryonic stem cells were obtained from ArunA Biomedicals (Athens, GA). Cells were expanded on tissue culture flasks pre-coated with either fibronectin (Sigma-Aldrich) or Matrigel (BD Biosciences), in proliferation medium consisting of AB2 basal neural medium, ANS neural supplement (both supplied by manufacturer), 10 ng/ml leukemia inhibitory factor (LIF; EMD Millipore), 20 ng/ml basic fibroblast growth factor (bFGF; R&D Systems), 2 mM GlutaMAX supplement (Life Technologies) and penicillin/streptomycin (Life Technologies). For neuronal differentiation experiments, cells were cultured in medium lacking bFGF.

ReNcell VM immortalized human neural progenitor cells derived from the ventral mesencephalon of human fetal brain were purchased from EMD Millipore. Cells were expanded on tissue culture flasks coated with laminin (Life Technologies), in media containing DMEM/F12 (Life Technologies), supplemented with B27 (Life Technologies), 2µg/ml heparin (StemCell Technologies), 20ng/ml bFGF (EMD Millipore), 20ng/ml EGF (Sigma) and penicillin/streptomycin (Life Technologies). For differentiation experiments, cells were cultured in medium lacking bFGF and EGF.

bioRxiv preprint doi: https://doi.org/10.1101/055533; this version posted August 25, 2017. The copyright holder for this preprint (which was not certified by peer review) is the author/funder, who has granted bioRxiv a license to display the preprint in perpetuity. It is made available under aCC-BY 4.0 International license.

Electrophysiology. For whole-cell patch clamp experiments, cultures were maintained in extracellular recording solution containing 119 mM NaCl, 5 mM KCl, 10 mM HEPES, 2 mM $CaCl_2$ and 1 mM $MgCl_2$, titrated to a pH of 7.3. Pipettes (5-10 MΩ) were pulled from standard borosilicate glass capillaries and back filled with intracellular recording solution containing 8 mM NaCl, 10mM KCl, 5 mM HEPES, 0.06 mM $CaCl_2$, 5 mM $MgCl_2$, 130 mM potassium gluconate and 0.6mM EGTA, titrated to a pH of 7.4. Recordings were performed using a MultiClamp 700A amplifier and a Digidata 1550 Data Acquisition System coupled with Clampex 10.4 software (Molecular Devices). Traces were analyzed in MATLAB.

In voltage-clamp experiments, cells were held at a holding potential of -50 mV and given a series of voltage steps from -90 to +100 mV. In current-clamp experiments, cells were held at approximately -70 mV through minimal current injection before application of a series of current steps ranging from -40 to +120 pA. Magnitudes of the current steps were modified according to the input resistance. Peak outward current amplitude was measured 40 ms after the initiation of the voltage sweep. Peak inward current was defined as the maximum transient negative current at any command voltage.

Immunocytochemistry. For immunostaining experiments, hNP1 cells were plated on Matrigel-coated 12 mm glass coverslips and differentiated as described earlier. Cultures were fixed with 4% paraformaldehyde for 15 min, permeabilized with 0.2% Triton-X and blocked with 6% goat serum for 1hr. Primary antibodies for Nestin and MAP2, followed by appropriate Alexa Fluor secondary antibodies were used. Nuclei were stained using Hoescht dye.

ReNcell VM cells were plated on laminin-coated LabTek chambered cover glasses (Fisher Scientific). Cultures were fixed with 4% paraformaldehyde for 15 min, permeabilized with 0.2% Triton-X and blocked

bioRxiv preprint doi: https://doi.org/10.1101/055533; this version posted August 25, 2017. The copyright holder for this preprint (which was not certified by peer review) is the author/funder, who has granted bioRxiv a license to display the preprint in perpetuity. It is made available under aCC-BY 4.0 International license.

with 10% goat serum for 1 hr. Primary antibodies for Tuj1, followed by appropriate Alexa Fluor secondary antibodies were used. Nuclei were stained using Hoescht dye.

See **Supplementary Table 2** for a list of antibodies and dilutions.

Image Acquisition and Segmentation. For all imaging experiments, hNP1 cells were plated at approximately 50% confluence on 12-well plates pre-coated with Matrigel and switched to differentiation medium 24 hours post-plating. Two datasets (biological replicates) were obtained by imaging the well plates at days 0, 3, 6, 9, 12 and 14 after withdrawal of bFGF from culture medium, using an automated stage Nikon Eclipse Ti-E Microscope. At the start of the experiment, five locations were chosen arbitrarily for each well, and the same locations were located and imaged at each time point. Imaging sessions lasted about 10 minutes and the plates were returned to the incubator after imaging. We also performed continuous imaging (**Supplementary Video 1**), for which the well plate was mounted on the stage of the microscope in a bold line cage incubator (Okolab) equipped with temperature control and gas flow rate control enabling a 37^0C 5% CO_2 environment. Images were acquired at 1-hour intervals for 8 days. In all time-lapse imaging experiments, 8-bit phase contrast images were acquired through a 10X objective (N.A. = 0.3) from a 1280 x 1080 pixel field of view using a Nikon DS-Qi1 camera. Physical pixel size was 0.64 µm.

Phase contrast image sequences were chosen for analysis based on the ability of a human observer to distinguish cellular features in the images. Images with large amounts of debris occluding cells were discarded manually. In this manner, a total of 16 and 14 image sequences for each of the 2 biologically independent datasets were chosen for analysis.

bioRxiv preprint doi: https://doi.org/10.1101/055533; this version posted August 25, 2017. The copyright holder for this preprint (which was not certified by peer review) is the author/funder, who has granted bioRxiv a license to display the preprint in perpetuity. It is made available under aCC-BY 4.0 International license.

Selected grayscale images were pre-processed by applying a median filter with a neighborhood of 3x3 pixels to remove noise and segmented using an unbiased intensity-gradient thresholding approach[33]. Starting from the grayscale image, the first derivative of the pixel intensity histogram was calculated. Fitting a linear function to the ascending portion of the first derivative and extrapolating to the x-axis resulted in a grayscale threshold, which was used to generate a binary image distinguishing cellular features from the background. Morphological operations performed on the binary image were:

1. Small objects of size lesser than 50 pixels were removed to filter out noise and other imaging artifacts.
2. Morphological opening was performed using a disk structuring element of radius 4 pixels. This was done to separate linear features (neurites), and circular features (cell bodies).
3. Cell bodies were separated using connected component labeling using the default 8-connected neighborhood.
4. Cell body objects smaller than 150 pixels and those touching the image border were removed.

All parameters used in image processing are listed in **Supplementary Table 1**.

In order to quantify the accuracy of our image processing algorithms, we compared the results with manual tracing of soma. These results showed a close agreement between the numbers of cells detected by our algorithm and by manual tracing at different time points (**Supplementary Figure 1**).

Calcium Imaging and Analysis

ReNcell VM cells were plated on laminin-coated LabTek chambered cover glasses for calcium imaging experiments. Cells were loaded with culture medium containing 3 µM of the fluorescent calcium indicator Fluo-4/AM (Life Technologies) and Pluronic F-127 (0.2% w/v, Life Technologies) for 30 min at 37°C. Imaging of spontaneous calcium activity was performed at 37°C using a 20X objective lens (N.A. = 0.75),

bioRxiv preprint doi: https://doi.org/10.1101/055533; this version posted August 25, 2017. The copyright holder for this preprint (which was not certified by peer review) is the author/funder, who has granted bioRxiv a license to display the preprint in perpetuity. It is made available under aCC-BY 4.0 International license.

with 488 nm excitation provided through a SOLA SE Light Engine (Lumencor). 16-bit fluorescence images were acquired at a sampling frequency of 1Hz for a total duration of 15 min, using a Zyla 5.5 sCMOS camera (Andor).

Following calcium imaging, samples were fixed with 4% paraformaldehyde and stained for nuclei using Hoescht dye. By navigating to the locations where calcium imaging was performed, manual co-registration was done to obtain nucleus images for the same fields of view.

Generation of Functional Networks from Calcium Imaging. Regions of interest (ROIs) were obtained by segmenting nucleus images using a local thresholding approach followed by the watershed algorithm. Undersegmented objects were algorithmically removed by discarding the top two percentile of object sizes obtained after segmentation.

Next, a time-varying fluorescence trace was calculated for each ROI. For each frame in the calcium fluorescence image stack, background (average pixel intensity of non-ROI regions in the image) was subtracted. Average fluorescence intensity for each ROI (F) was obtained by averaging pixel intensity values within the ROI for each time point. Baseline fluorescence (F_0) for each ROI was calculated as the minimum intensity value in a window 90s before and after each time point. The normalized fluorescence trace for the ROI was then calculated as $F - F_0/F_0$. Cells with low activity were filtered out by discarding traces with less than three peaks. The remaining traces were manually inspected to ensure that low-activity cells were not included in the analysis. This was done to avoid false positives in the cross-correlation analysis.

bioRxiv preprint doi: https://doi.org/10.1101/055533; this version posted August 25, 2017. The copyright holder for this preprint (which was not certified by peer review) is the author/funder, who has granted bioRxiv a license to display the preprint in perpetuity. It is made available under aCC-BY 4.0 International license.

Functional networks were created following the method described by Smedler et al[34], where cross-covariance between signals is used to assign functional connections between pairs of cells. A randomized dataset was generated by shuffling each signal in the original dataset at a random time point. The 99th percentile of cross-covariance values for the randomized dataset was used as a threshold for determining significant correlations.

Creation of Spatial Graphs. Spatial graphs were created from microscope images using cytoNet, software developed in-house[35]. For each pair of objects (soma/nuclei), a threshold distance for proximity was defined as the average of the two object diameters, multiplied by a scaling factor (S). If the Euclidean distance between the object centroids was lower than the threshold distance computed, then the pair of objects was connected with a "proximity edge" (**Figure 2j, k**). We chose a scaling factor of 2 for phase contrast images and 3 for nucleus immunofluorescence images based on similarity in network density for the resulting networks (**Supplementary Figure 2**).

Metric Computation. All the network metrics described in Table 1 were computed using cytoNet[35]. It is to be noted that not all metrics derived from graph theory have a ready biological interpretation, especially in the context of spatial graphs. For example, interpretation of metrics like degree-degree correlations and rich-club metric (**Supplementary Figure 4**) are limited, due to the implicit limit in the type of connections that are possible in spatial graphs. Keeping this in mind, we analyzed metrics with an intuitive biological interpretation, i.e., information flow and connectivity.

Random graphs were constructed through degree-preserving rewiring, maintaining the degree distribution of the original graph (**Supplementary Figure 3**). Each link (edge) belonging to any given node in the original graph was randomly re-assigned to a node that was chosen from all possible nodes with

bioRxiv preprint doi: https://doi.org/10.1101/055533; this version posted August 25, 2017. The copyright holder for this preprint (which was not certified by peer review) is the author/funder, who has granted bioRxiv a license to display the preprint in perpetuity. It is made available under aCC-BY 4.0 International license.

uniform probability. Metrics computed for random graphs were averaged across 100 different realizations of the random graphs. This mode of random graph generation was chosen to eliminate finite-size effects inherent in other models of random graphs such as Erdõs-Rényi random graphs. To ensure robustness of the network metrics, we tested varying fields of view for the images, and confirmed the trends remained consistent (**Supplementary Figure 5**).

ACKNOWLEDGEMENTS

We thank Dr. Byron Long, Dr. David Noren, Dr. André Schultz, Chenyue Wendy Hu and Dr. Ka Wai Lin for helpful discussions and comments on the manuscript, Hanyang Li and Kylie Balotin for assistance with manual tracing of cells, Daniel Murphy and Dr. Guillaume Duret for technical assistance. This work was supported by NSF Career Grant 1150645 to A.A.Q. and NSF Neural and Cognitive Systems grant 1533708 to A.A.Q. and J.T.R. A.S.M. was supported through NSF IGERT training grant 1250104.

AUTHOR CONTRIBUTIONS

All authors designed the experiments. A.S.M. performed the experiments. A.A.Q., A.S.M. and N.E.G. analyzed the data. All authors contributed to writing the manuscript. A.A.Q. and J.T.R. supervised the work.

COMPETING FINANCIAL INTERESTS

The authors declare no competing financial interests.

REFERENCES

1. Bullmore, E. & Sporns, O. Complex brain networks: graph theoretical analysis of structural and functional systems. *Nat Rev Neurosci* **10,** 186–198 (2009).

bioRxiv preprint doi: https://doi.org/10.1101/055533; this version posted August 25, 2017. The copyright holder for this preprint (which was not certified by peer review) is the author/funder, who has granted bioRxiv a license to display the preprint in perpetuity. It is made available under aCC-BY 4.0 International license.

2. Bassett, D. S. & Sporns, O. Network neuroscience. *Nat. Neurosci.* **20,** 353–364 (2017).

3. Schröter, M., Paulsen, O. & Bullmore, E. T. Micro-connectomics: probing the organization of neuronal networks at the cellular scale. *Nat. Rev. Neurosci.* **18,** 131–146 (2017).

4. Feldt, S., Bonifazi, P. & Cossart, R. Dissecting functional connectivity of neuronal microcircuits: experimental and theoretical insights. *Trends Neurosci.* **34,** 225–36 (2011).

5. Shefi, O., Ben-Jacob, E. & Ayali, A. Growth morphology of two-dimensional insect neural networks. *Neurocomputing* **44–46,** 635–643 (2002).

6. de Santos-Sierra, D. *et al.* Emergence of small-world anatomical networks in self-organizing clustered neuronal cultures. *PLoS One* **9,** e85828 (2014).

7. Downes, J. H. *et al.* Emergence of a small-world functional network in cultured neurons. *PLoS Comput. Biol.* **8,** e1002522 (2012).

8. Lefort, S., Tomm, C., Floyd Sarria, J.-C. & Petersen, C. C. H. The Excitatory Neuronal Network of the C2 Barrel Column in Mouse Primary Somatosensory Cortex. *Neuron* **61,** 301–316 (2009).

9. Yassin, L. *et al. An Embedded Subnetwork of Highly Active Neurons in the Neocortex*. *Neuron* **68,** (2010).

10. Gal, E. *et al.* Rich cell-type-specific network topology in neocortical microcircuitry. *Nat. Neurosci.* **20,** 1004–1013 (2017).

11. ffrench-Constant. The neural stem cell microenvironment. *StemBook* 1–26 (2008). doi:10.3824/stembook.1.15.1

12. Malmersjö, S. *et al.* Neural progenitors organize in small-world networks to promote cell proliferation. *Proc. Natl. Acad. Sci. U. S. A.* **110,** E1524-32 (2013).

13. Spitzer, N. C. Electrical activity in early neuronal development. *Nature* **444,** 707–12 (2006).

14. Blankenship, A. G. & Feller, M. B. Mechanisms underlying spontaneous patterned activity in developing neural circuits. *Nat. Rev. Neurosci.* **11,** 18–29 (2010).

bioRxiv preprint doi: https://doi.org/10.1101/055533; this version posted August 25, 2017. The copyright holder for this preprint (which was not certified by peer review) is the author/funder, who has granted bioRxiv a license to display the preprint in perpetuity. It is made available under aCC-BY 4.0 International license.

15. Watters, A. K. *et al.* Identification and dynamic regulation of tight junction protein expression in human neural stem cells. *Stem Cells Dev.* **24,** 1377–89 (2015).

16. Edri, R. *et al.* Analysing human neural stem cell ontogeny by consecutive isolation of Notch active neural progenitors. *Nat. Commun.* **6,** 6500 (2015).

17. Shimojo, H., Ohtsuka, T. & Kageyama, R. Oscillations in Notch Signaling Regulate Maintenance of Neural Progenitors. *Neuron* **58,** 52–64 (2008).

18. Suzuki, I. K. & Vanderhaeghen, P. Is this a brain which I see before me? Modeling human neural development with pluripotent stem cells. *Development* **142,** 3138–3150 (2015).

19. Gage, F. H. Mammalian Neural Stem Cells. *Science (80-.).* **287,** 1433–1438 (2000).

20. Bounova, G. & De Weck, O. Overview of metrics and their correlation patterns for multiple-metric topology analysis on heterogeneous graph ensembles. *Phys. Rev. E - Stat. Nonlinear, Soft Matter Phys.* **85,** (2012).

21. Watts, D. J., Watts, D. J., Strogatz, S. H. & Strogatz, S. H. Collective dynamics of 'small-world' networks. *Nature* **393,** 440–2 (1998).

22. Colizza, V., Flammini, A., Serrano, M. A. & Vespignani, A. Detecting rich-club ordering in complex networks. **2,** 110–115 (2006).

23. Newman, M. Assortative Mixing in Networks. *Phys. Rev. Lett.* **89,** 208701 (2002).

24. Zhou, Z.-D., Kumari, U., Xiao, Z.-C. & Tan, E.-K. Notch as a molecular switch in neural stem cells. *IUBMB Life* **62,** 618–623 (2010).

25. Androutsellis-Theotokis, A. *et al.* Notch signalling regulates stem cell numbers in vitro and in vivo. *Nature* **442,** 823–826 (2006).

26. Andersson, E. R., Sandberg, R. & Lendahl, U. Notch signaling: simplicity in design, versatility in function. *Development* **138,** 3593–3612 (2011).

27. Sun, B., Lembong, J., Normand, V., Rogers, M. & Stone, H. A. Spatial-temporal dynamics of

bioRxiv preprint doi: https://doi.org/10.1101/055533; this version posted August 25, 2017. The copyright holder for this preprint (which was not certified by peer review) is the author/funder, who has granted bioRxiv a license to display the preprint in perpetuity. It is made available under aCC-BY 4.0 International license.

collective chemosensing. *Proc. Natl. Acad. Sci. U. S. A.* **109,** 7753–8 (2012).

28. Friedl, P. & Gilmour, D. Collective cell migration in morphogenesis, regeneration and cancer. *Nat. Rev. Mol. Cell Biol.* **10,** 445–457 (2009).

29. Yu, Y.-C., Bultje, R. S., Wang, X. & Shi, S.-H. Specific synapses develop preferentially among sister excitatory neurons in the neocortex. *Nature* **458,** 501–4 (2009).

30. Butt, S. J. B. *et al.* The Temporal and Spatial Origins of Cortical Interneurons Predict Their Physiological Subtype. *Neuron* **48,** 591–604 (2005).

31. Kageyama, R., Ohtsuka, T., Shimojo, H. & Imayoshi, I. Dynamic regulation of Notch signaling in neural progenitor cells. *Curr. Opin. Cell Biol.* **21,** 733–740 (2009).

32. Pfeuty, B. A computational model for the coordination of neural progenitor self-renewal and differentiation through Hes1 dynamics. *Development* **142,** 477–485 (2015).

33. Curl, C. *et al.* Quantitative phase microscopy: a new tool for measurement of cell culture growth and confluency in situ. *Pflügers Arch. - Eur. J. Physiol.* **448,** 462–468 (2004).

34. Smedler, E., Malmersjö, S. & Uhlén, P. Network analysis of time-lapse microscopy recordings. *Front. Neural Circuits* **8,** 111 (2014).

35. Mahadevan, A. S. *et al.* cytoNet: Network Analysis of Cell Communities. *bioRxiv* (2017). at <http://www.biorxiv.org/content/early/2017/08/24/180273>

bioRxiv preprint doi: https://doi.org/10.1101/055533; this version posted August 25, 2017. The copyright holder for this preprint (which was not certified by peer review) is the author/funder, who has granted bioRxiv a license to display the preprint in perpetuity. It is made available under aCC-BY 4.0 International license.

Supplementary Information

Living Neural Networks: Dynamic Network Analysis of Developing Neural Stem Cells

Arun S. Mahadevan, Nicolas E. Grandel, Jacob T. Robinson, Amina A. Qutub

Supplementary Figure 1	Comparison of automated image segmentation and manual tracing of soma
Supplementary Figure 2	Results of analysis with different scaling factors
Supplementary Figure 3	Random graph generation through degree-preserving rewiring
Supplementary Figure 4	Trends in network metrics
Supplementary Figure 5	Scale invariance of network metrics
Supplementary Figure 6	Immunostaining of ReNcell cultures at days 1, 3 and 5
Supplementary Figure 7	Cross-correlation analysis to infer functional connectivity from calcium imaging data
Supplementary Table 1	List of parameters in image processing
Supplementary Table 2	List of antibodies used for immunocytochemistry
Supplementary Video 1	8-day time-lapse movie of differentiating hNP1 cells
Supplementary Video 2	Image-processed frames from Supplementary Video 1
Supplementary Video 3	Calcium imaging movie from day 1 ReNcell culture
Supplementary Video 4	Calcium imaging movie from day 3 ReNcell culture overlaid with immunostaining for neurons and glial cells
Supplementary Video 5	Calcium imaging movie from day 5 ReNcell culture overlaid with immunostaining for neurons and glial cells

bioRxiv preprint doi: https://doi.org/10.1101/055533; this version posted August 25, 2017. The copyright holder for this preprint (which was not certified by peer review) is the author/funder, who has granted bioRxiv a license to display the preprint in perpetuity. It is made available under aCC-BY 4.0 International license.

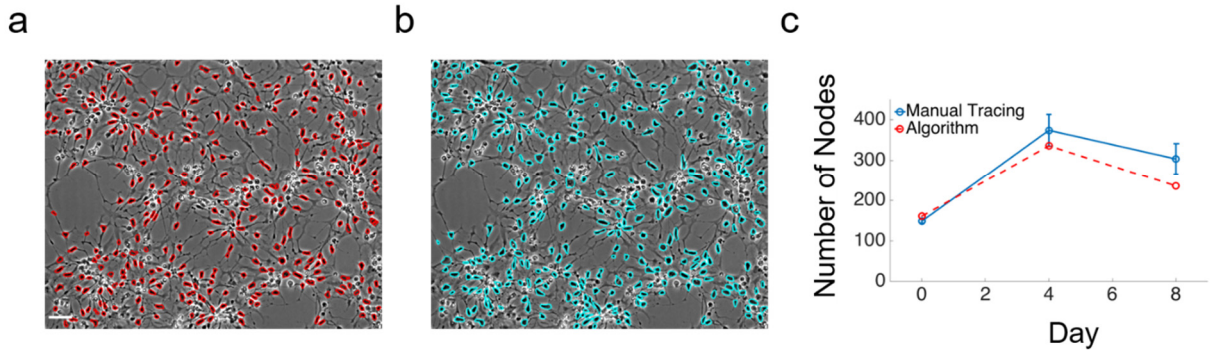

Supplementary Figure 1

Comparison of automated image segmentation and manual tracing of soma (a) Image at day 4 with soma outlines picked out by algorithm outlined in red; scale bar = 50 µm. **(b)** Same image in (a), with manual tracing of soma outlined in cyan. **(c)** Comparison of number of soma picked out by algorithm and manual tracing by 3 independent observers. Error bars indicate SEM.

bioRxiv preprint doi: https://doi.org/10.1101/055533; this version posted August 25, 2017. The copyright holder for this preprint (which was not certified by peer review) is the author/funder, who has granted bioRxiv a license to display the preprint in perpetuity. It is made available under aCC-BY 4.0 International license.

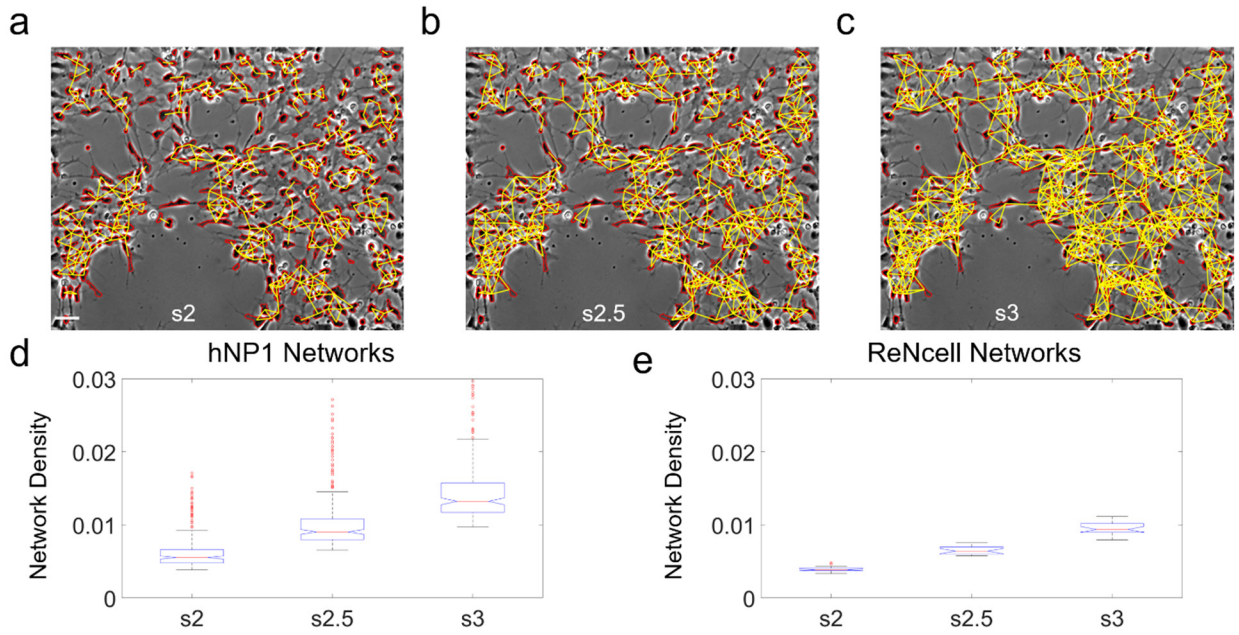

Supplementary Figure 2

Scaling factor analysis

(a-c) hNP1 image at day 3 with graph representations using different scaling factors; scale bar = 50 µm. **(a)** scaling factor = 2; soma boundaries are outlined in red, and proximity edges are shown in yellow (scale bar = 50µm). **(b)** scaling factor = 2.5 **(c)** scaling factor = 3. **(d)** Boxplot of network density for all hNP1 networks. **(e)** Box plot of network density for all ReNcell networks. Scaling factors s2 and s3 were chosen for hNP1 and ReNcell networks based on similarity in overall network density.

bioRxiv preprint doi: https://doi.org/10.1101/055533; this version posted August 25, 2017. The copyright holder for this preprint (which was not certified by peer review) is the author/funder, who has granted bioRxiv a license to display the preprint in perpetuity. It is made available under aCC-BY 4.0 International license.

a

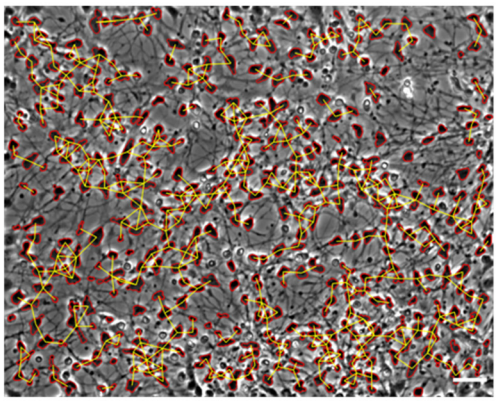

b

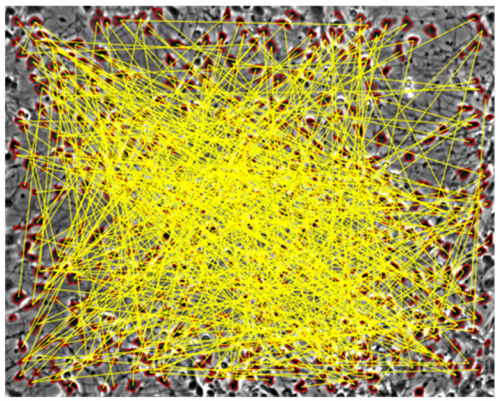

c

Network Efficiency (E)	Network Efficiency of random graph (E_{rand})	Clustering Coefficient (C)	Clustering Coefficient of random graph (C_{rand})
0.0282	0.1158	0.3070	0.0037

Supplementary Figure 3

Random graph generation through degree-preserving rewiring

(a) Original graph representation of day 14 image. Soma are outlined in red and edges are shown in yellow; scale bar = 50 µm. **(b)** Random graph generated by rewiring nodes in panel A with uniform probability. **(c)** Network parameters for graphs in (a) and (b).

bioRxiv preprint doi: https://doi.org/10.1101/055533; this version posted August 25, 2017. The copyright holder for this preprint (which was not certified by peer review) is the author/funder, who has granted bioRxiv a license to display the preprint in perpetuity. It is made available under aCC-BY 4.0 International license.

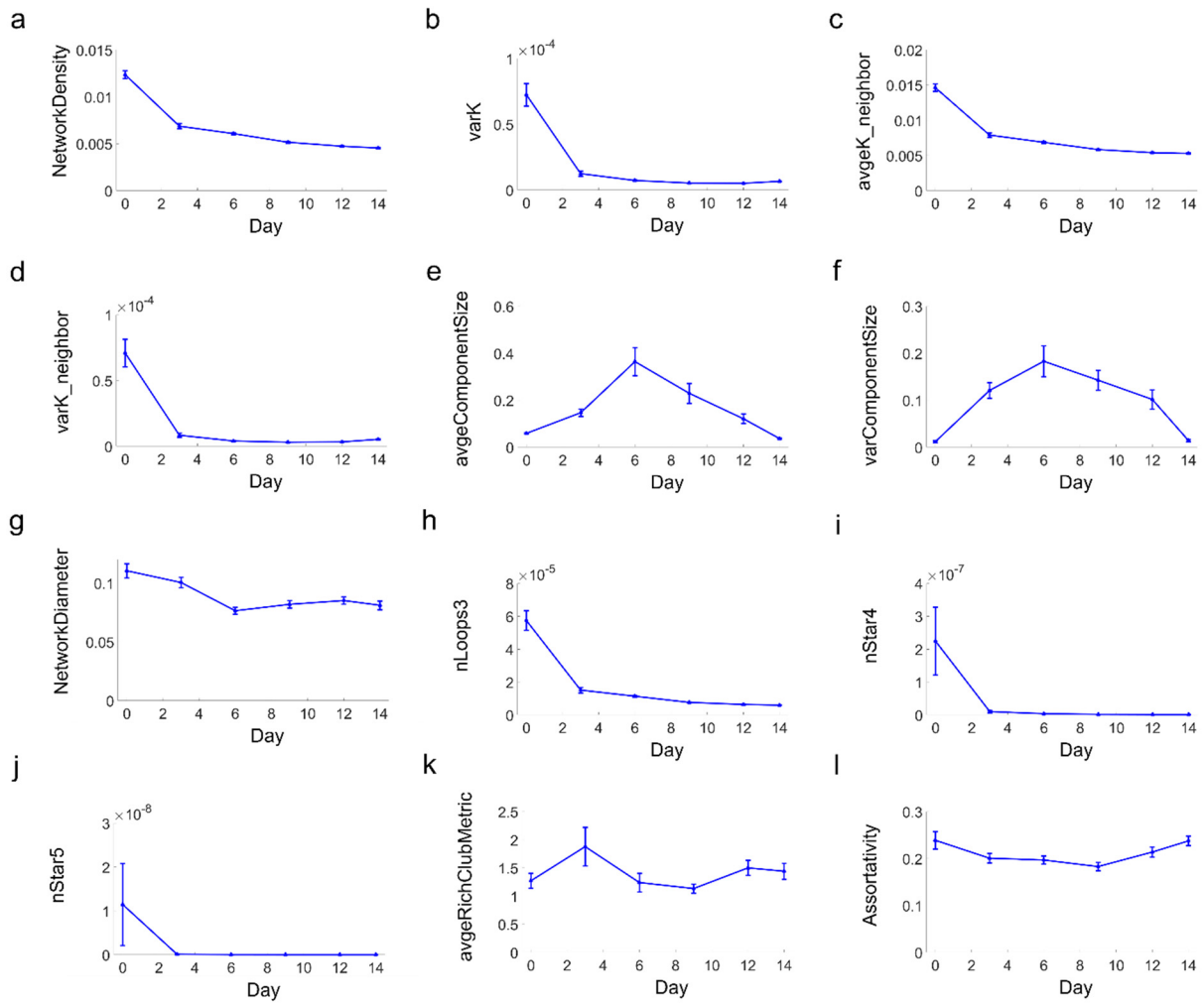

Supplementary Figure 4

Trends in network metrics in hNP1 cultures

(a) Network Density. **(b)** Variance in Degree. **(c)** Average Degree. **(d)** Variance in Neighbor Degree. **(e)** Average component size. **(f)** Variance in Component Size. **(g)** Network Diameter. **(h)** Triangular Loop Count. **(i)** 5-Star Motif Count. **(j)** 6-Star Motif Count. **(k)** Rich-Club Metric Average. **(l)** Assortativity.

bioRxiv preprint doi: https://doi.org/10.1101/055533; this version posted August 25, 2017. The copyright holder for this preprint (which was not certified by peer review) is the author/funder, who has granted bioRxiv a license to display the preprint in perpetuity. It is made available under aCC-BY 4.0 International license.

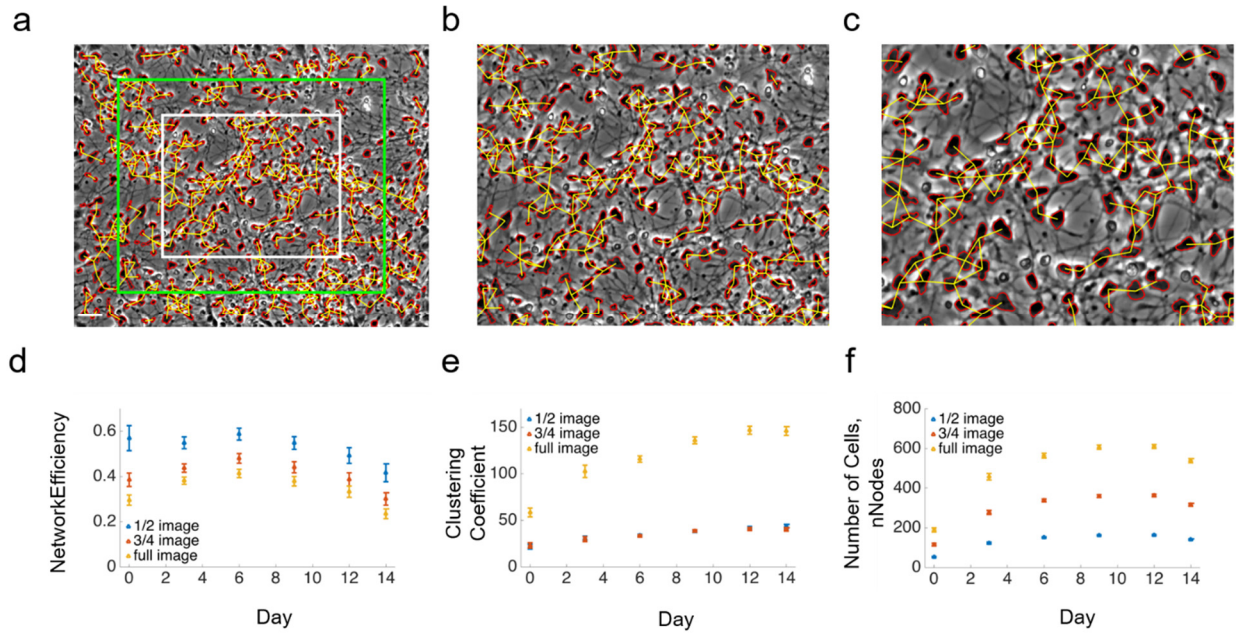

Supplementary Figure 5

Scale invariance of network metrics

(a-c) Different fields of view chosen for analysis. **(a)** Image at day 14; green box represents 75% of the field of view, white box represents 50% of the field of view (scale bar = 50µm). **(b)** Green inset from panel A. **(c)** White inset from (a). **(d-f)** Graph-based metrics computed for full image, 75% of the image and 50% of the image. **(d)** Network Efficiency across time. **(e)** Clustering coefficient. **(f)** Total number of cells in field of view. Values are reported as the mean across N = 30 networks $\pm$ SEM.

bioRxiv preprint doi: https://doi.org/10.1101/055533; this version posted August 25, 2017. The copyright holder for this preprint (which was not certified by peer review) is the author/funder, who has granted bioRxiv a license to display the preprint in perpetuity. It is made available under aCC-BY 4.0 International license.

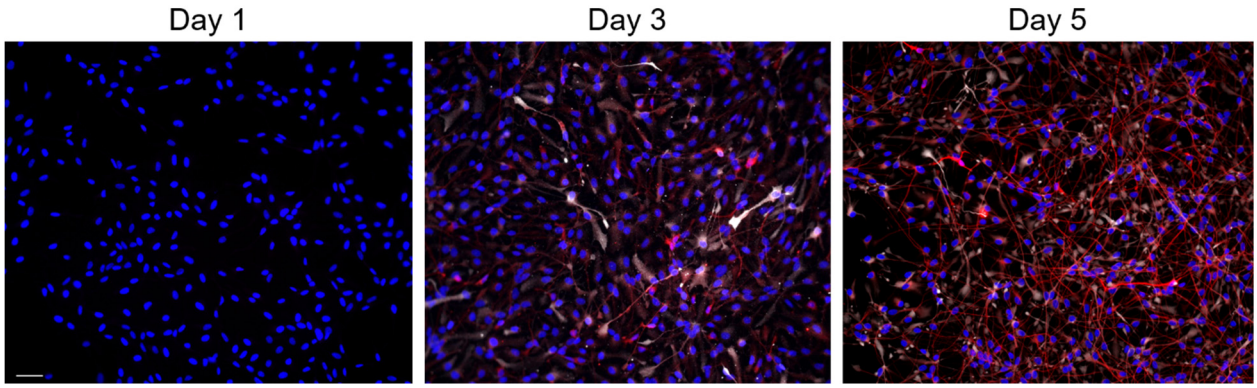

Supplementary Figure 6

Immunostaining of ReNcell reveals differentiation into neurons and glia.

β(III) tubulin (red) marks differentiated neurons, GFAP (white) marks differentiated glial cells. Nuclei are stained with Hoescht (blue); scale bar = 50 µm.

bioRxiv preprint doi: https://doi.org/10.1101/055533; this version posted August 25, 2017. The copyright holder for this preprint (which was not certified by peer review) is the author/funder, who has granted bioRxiv a license to display the preprint in perpetuity. It is made available under aCC-BY 4.0 International license.

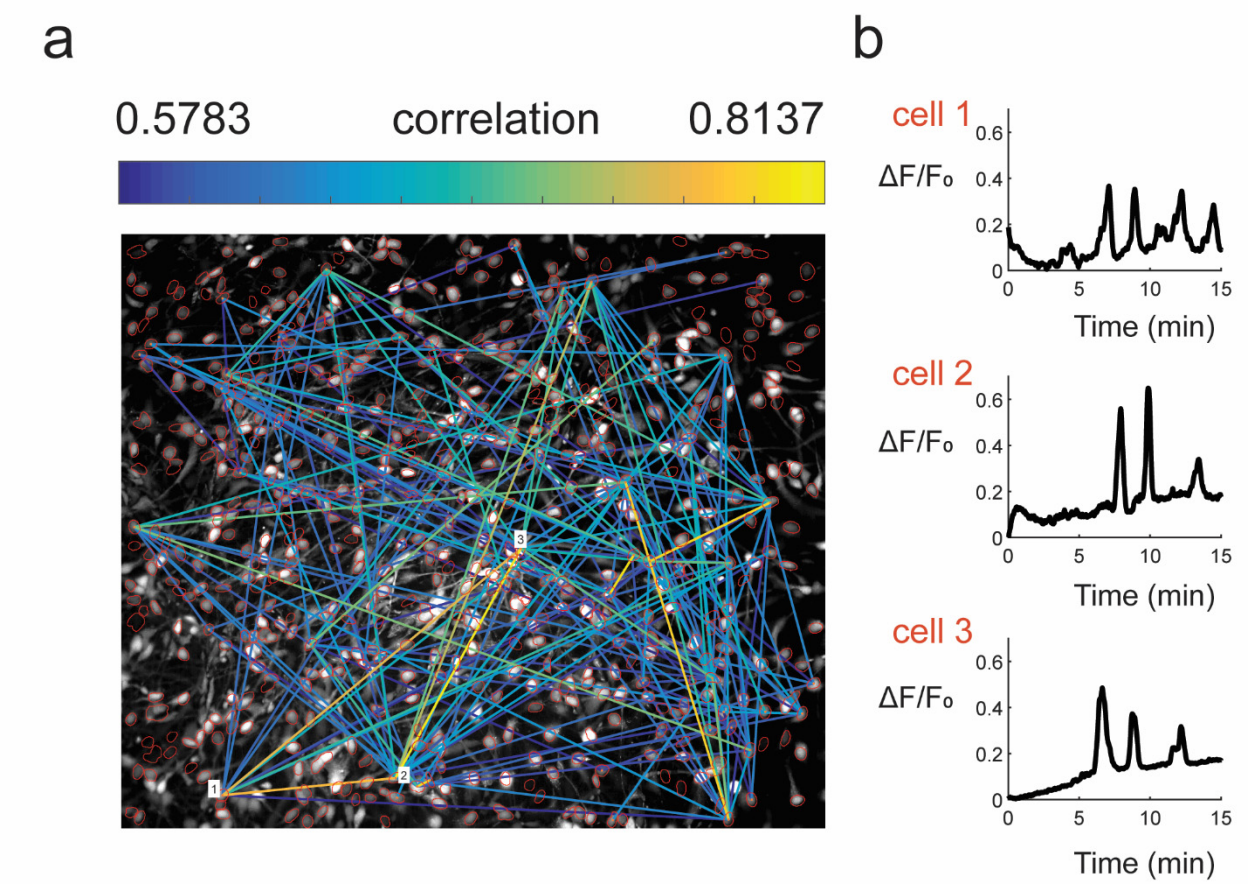

Supplementary Figure 7

Cross-correlation analysis to infer functional connectivity from calcium imaging data.

(a) Maximum intensity image from day 3 ReNcell culture loaded with Fluo-4 for calcium imaging. Inferred functional network is overlaid on the image, with correlation magnitude represented by edge color heatmap. ROIs obtained from corresponding nucleus image are shown in red. **(b)** Normalized calcium traces from 3 highly correlated cells marked in (a) are shown.

bioRxiv preprint doi: https://doi.org/10.1101/055533; this version posted August 25, 2017. The copyright holder for this preprint (which was not certified by peer review) is the author/funder, who has granted bioRxiv a license to display the preprint in perpetuity. It is made available under aCC-BY 4.0 International license.

Supplementary Table 1. List of parameters in image processing for hNP1 phase contrast images.

Parameter Description	Parameter Value
Size of median filtering neighborhood	3 pixels x 3 pixels
First threshold for removing small particles	50 pixels
Second threshold for removing small particles (after separation of cell body objects)	150 pixels
Radius of disk used for morphological opening	4 pixels
Neighborhood connectivity used for connected component labeling	8-connected neighborhood

Supplementary Table 2. List of antibodies used for immunocytochemistry.

Antibody	Host	Supplier	Catalog Number	Dilution
Anti-Nestin	Mouse	Neuromics	MO15012	1:200
Anti-MAP2	Rabbit	Millipore	AB5622	1:500
Anti-Tuj1	Mouse	R&D Systems	MAB1195	1:500
Anti-GFAP	Chicken	Abcam	ab4674	1:1000
Alexa Fluor anti-mouse 488, anti-rabbit 594, anti-mouse 594, anti-chicken 647	Goat	Life Technologies, Abcam	A-21121, A-11037, A-11005, ab150171	1:1000

bioRxiv preprint doi: https://doi.org/10.1101/055533; this version posted August 25, 2017. The copyright holder for this preprint (which was not certified by peer review) is the author/funder, who has granted bioRxiv a license to display the preprint in perpetuity. It is made available under aCC-BY 4.0 International license.

Supplementary Video 1. 8-day time-lapse movie of differentiating hNP1 human neural progenitor cells.

Supplementary Video 2. Same image sequence as in Supplementary Video 1, with cell bodies detected through image processing outlined in red and proximity edges shown in yellow.

Supplementary Video 3. Calcium imaging movie from day 1 ReNcell culture. Movie is sped up 50X. Original video was captured with a frame rate of 1Hz for a total duration of 15min.

Supplementary Video 4. Calcium imaging movie from day 3 ReNcell culture. Movie is sped up 50X. Original video was captured with a frame rate of 1Hz for a total duration of 15 min. Green channel represents Fluo-4, and other channels represent immunostain signal from fixed culture overlaid on calcium video. Blue is the nuclear stain from Hoescht dye, red is Tuj1 and white is GFAP.

Supplementary Video 5. Calcium imaging movie from day 5 ReNcell culture. Movie is sped up 50X. Original video was captured with a frame rate of 1Hz for a total duration of 15 min. Green channel represents Fluo-4, and other channels represent immunostain signal from fixed culture overlaid on calcium video. Blue is the nuclear stain from Hoescht dye and red is Tuj1.